Unveiling the role of β-Ag₂MoO₄ microcrystals to the improvement of antibacterial activity

Camila Cristina De Foggi[a], Regiane Cristina De Oliveira[b], Marcelo Assis[b], Maria Tereza Fabbro[b], Valmor Roberto Mastelaro[c], Carlos Eduardo Vergani[a], Lourdes Gracia[d], Juan Andrés[d], Elson Longo[b] and Ana Lucia Machado[a].

[a]São Paulo State University (UNESP). Department of Dental Materials and Prosthodontics, 14801-907, Brazil

[b]Interdisciplinary Laboratory of Electrochemistry and Ceramics, University Federal of São Carlos, P.O. Box 676, 13565-905 São Carlos, SP, Brazil.

[c]São Carlos Institute of Physics, University of São Paulo, CP 369, São Carlos 13560-970, São Paulo, Brazil

[d]Department of Physic and Analytical Chemistry, Universitat Jaume I, Campus Riu Sec, E-12071 Castellón, Spain

Abstract

Crystal morphology with different surfaces is important for improving the antibacterial activity of materials. In this experimental and theoretical study, the antibacterial activity of β-Ag₂MoO₄ microcrystals against the Gram-positive bacteria, namely, methicillin-resistant *Staphylococcus aureus* (MRSA), and the Gram-negative bacteria, namely, *Escherichia coli* (*E.coli*), was investigated. In this study, β-Ag₂MoO₄ crystals with different morphologies were synthetized by a simple co-precipitation method using three different solvents. The antimicrobial efficacy of the obtained

microcrystals against both bacteria increased according to the solvent used in the following order: water <ammonia<ethanol.

Supported by experimental evidence, a correlation between morphology, surface energy, and antibacterial performance was established. By using the theoretical Wulff construction, which was obtained by means of density functional calculations, the morphologies with large exposition of the (001) surface exhibited superior antibacterial activity. This study provides a low cost route for synthesizing β-Ag$_2$MoO$_4$ crystals and a guideline for enhancing the biological effect of biocides on pathogenic bacteria by the morphological modulation.

Keywords: β-Ag$_2$MoO$_4$, antibacterial activity, morphology evolution

Introduction

Metal molybdates such as A$_x$MoO$_z$ (where A is a monovalent, divalent, or trivalent metal ion) have recently been investigated intensively [1,2,11,12,3–10] owing to their chemical stability and unique crystal structure (layers of molybdenum oxide octahedra separated by the metal ions) [13], which make them suitable for a wide range of applications. Particularly, silver molybdates have been investigated in the fields of lubrication [14,15], humidity and gas sensors [16,17], surface enhanced Raman scattering techniques [18,19], photocatalysis [11–13,20,21], and photoluminescence [20,22,23]. A plethora of synthetic methods have been used to harness these applications, such as hydrothermal [19,24–27], solution-based chemical reaction [18], co-precipitation [23,28], dynamic template route [21], laser annealing [29], and microwave-assisted hydrothermal methods [20,30]. In this context, Ng and Fan [31] have recently reported the preparation of β-Ag$_2$MoO$_4$ crystals with high-index facets via

the delicate tuning of the supersaturation conditions during crystal growth. Additionally, they were able to find a relationship between morphology and photocatalytic activity.

The morphological modulations can be achieved by the different solvents (water, ammonia, and ethanol) used in the co-precipitation synthesis method, as we described previously [28].

As a continuation of our work in this field of research, in this paper, we report the antibacterial activity of β-Ag_2MoO_4 microcrystals against gram-positive bacteria, namely, methicillin-resistant *Staphylococcus aureus* (MRSA), and gram-negative bacteria, namely, *Escherichia coli* (*E. coli*). These bacteria are important because they are opportunistic pathogens that are often inherently resistant to antibiotics or capable of rapidly building resistance to many common antimicrobial agents [32]. More significantly, the biological effects of β-Ag_2MoO_4 with different morphologies on the bacteria are systematically discussed. Additionally, to gain a deeper understanding of the atomic and electronic structure, and to establish a correlation among the morphology, surface energy, optical properties, and antibacterial activities, we conducted first principle calculations on the basis of density functional theory (DFT) to complement our experimental findings. This study intends to provide a more comprehensive insight into the development of novel biocide with a unique morphology and future potential for use in biological applications.

Results and Discussion

The β-Ag_2MoO_4 microcrystals were synthesized by using different solvents (water, ammonia, and ethanol) and the co-precipitation method. The experimental method is described in the Supplementary Material (SM) section. The samples were structurally characterized by x-ray (XRD) diffraction to evaluate the order/disorder at

long range. Figure 1 shows the XRD for the samples of silver molybdate. It was observed that all compounds presented a structure type assigned to a cubic spinel with the Fd3m space group, which is in agreement with the *Inorganic Crystal Structure Database* (ICSD) card 238013 [20]. The lattice parameters for the β-Ag_2MoO_4 phase are a = b = c = 9.3170 Å and a = b = c 90 °. Moreover, Figure 1 shows clearly that there was no other additional peak; that is, there was no undesirable secondary phase. Figure 1 shows the cubic spinel structure type that was composed by distorted octahedral clusters [AgO_6] with Oh symmetry for the Ag sites, and distorted tetrahedral clusters [MoO_4] with Td symmetry for the Mo sites. The crystallinity degree of a structure (order/disorder), that is, the organization at long range is directly dependent of the manner of the ions organize themselves into the structure, being that it is totally dependent on the chemical environment in which the material is formed. Therefore, the change of solvent, or the addition of any species in the synthesis of the material may corroborate a change in the order/disorder. A factor related to structural order/disorder effects at long-range can be found by the analysis of the full width at half maximum (FWHM) of the most intense peak of the XRD patterns, related to the plane (311) of the β-Ag_2MoO_4. The samples obtained in water, alcohol and ammonia, have FMHW values of 0.18, 0.21 and 0.23° respectively, showing that the samples synthesized with alcohol and ammonia have a lower degree of order than the samples obtained in water.

<Figure 1>

Figure 1: XRD patterns of the β-Ag_2MoO_4 microcrystals synthesized in water, alcohol and ammonia.

<Figure 2>

Figure 2: Raman (2a) and FT-IR (2b) spectra of the β-Ag₂MoO₄ microcrystals synthesized in water, alcohol and ammonia.

Raman spectroscopy is a technique complementary to XRD for estimating structural order/disorder at short-range. Figure 2 shows the experimental spectra obtained for all samples. The β-Ag₂MoO₄ belongs to the point-group symmetry O_h^7 with the centrosymmetric inversion, which indicates five active Raman modes (A₁g, Eg, and T₂g) obtained from the decomposition of point Γ (Γ = A₁g + Eg + 3T₂g + T₁g) [20]. Figure 2a shows the spectra for the samples obtained in different solvents. The spectra of all samples show four characteristic peaks centered at 276, 355, 761, and 873 cm⁻¹. The first Raman mode at 276 cm⁻¹ is associated with a transition Eg, which refers to external structure vibrations on the [AgO₆] clusters [20]. The Raman mode at 355 cm⁻¹ was associated with the transition T₂g caused by the O-Mo-O asymmetric bending vibrations [20,33]. Both the 761 and 873 cm⁻¹ modes are associated with the T₂g and A₁g transitions, respectively, and were caused by the asymmetric and symmetric O-Mo-O vibrations [20,33]. Figure 2b shows shows FT-IR for the samples of β-Ag₂MoO₄. In the FT-IR spectra of the samples the band at 827 cm⁻¹ is observed related to a asymmetrical stretching of the O-Mo-O bonds of the [MoO₄] tetrahedral clusters [11,34]. Other vibrations are not observed because they appear below 400 cm⁻¹, outside the limit of the equipment used.

Theoretical investigations based on first principle calculations by *ab-initio* and quantum-chemical simulations have been increasingly used to complement the experimental findings, provide valuable information of the electronic, structural, and energetic properties, and simulate and predict the morphology of the materials [20,33,35]. Thus, by using this combined experimental and theoretical approach,

previous studies determined that the most stable morphology for the β-Ag_2MoO_4 can occur when the surface energies are 1.90,1.28, and 3.46 J/m^2 for the (001), (011), and (111) faces, respectively [28,33].

Considering that Ag_2MoO_4 acquires different morphologies according to the synthetic method employed [28,30], in this study, the morphologies of the β-Ag_2MoO_4 samples were investigated by field emission scanning electron microscopy (FE-SEM), and are of fundamental importance to understanding the morphological evolution process and changes in the surfaces of the crystals with the variations of the used solvents. The β-Ag_2MoO_4 samples that were obtained by using different solvents are shown in Figure 3. The predominant morphologies obtained experimentally display the exposed (001), (011), and (111) surfaces, which support the hypothesis that these surfaces are stabilized by interacting with the solvent molecules. This observation suggests that the Wulff shape of β-Ag_2MoO_4 is closely related to the chemical environment.

<Figure 3>

Figure 3: FE-SEM images, morphologies, and facets of the β-Ag_2MoO_4 samples obtained by using different solvents: (a) water, (b) alcohol, and (c) ammonia.

For the following discussion on the relationship between the morphology-antibacterial activity of the β-Ag_2MoO_4 samples to be valid, it is assumed that the structure and facet composition of the crystals are preserved in the time scale of the experiments. The Wulff crystal representation of the optimized β-Ag_2MoO_4, and the available morphologies that would be obtained by assuming different values for the surface energies of the three facets are displayed in Figure 4. By analyzing Figure 4, it can be seen that the experimental and theoretical morphologies are in good agreement:

(a) when water was used as the solvent, the surface energy of the (111) surface decreased from 3.46 to 1.28 J/m^2; (b) when ammonia was used as the solvent; the surface energy of the (111) surface decreased from 3.46 to 1.28 J/m^2, and the surface energy of the (001) surface decreased from 1.90 to 1.5 J/m^2;(c) when ethanol was used as the solvent, the surface energy values of both the (111) and (001) surfaces decreased to 1.28 J/m^2.

<Figure 4>

Figure 4: Map of available β-Ag$_2$MoO$_4$morphologies based on Wulff crystal construction as function of surface energy values.

The minimum inhibitory concentrations (MICs), which are defined as the lowest concentrations required for complete growth inhibition (no visible growth by visual inspection), and the minimum bacterial concentrations (MBCs), which are defined as the lowest concentrations that do not result in bacterial growth on plates, were determined for the β-Ag$_2$MoO$_4$ microcrystals that were synthesized in different solvents (water, ammonia, and ethanol). The tests were performed according to the standard methods described in Clinical Laboratory Standards Institute (CLSI) [36]. The microorganisms evaluated in this study were MRSA (ATCC 33591) and *E. coli* (ATCC 8739). In the microbiological test results shown in Figure 5, the MIC value was the same as the MBC value for MRSA for the three solvents used in the synthesis of the β-Ag$_2$MoO$_4$. Similar findings were observed for *E. coli*.

<Figure 5>

Figure 5: Summary of log$_{10}$ CFU/mL MRSA values (a) and *E. coli* (b) obtained for sub-inhibitory concentrations of the β-Ag$_2$MoO$_4$synthesized in water, ammonia, and ethanol. Control MRSA = 8.8 (± 0.71) log$_{10}$ CFU/mL; control *E. coli* = 7.3 (± 0.20) log$_{10}$ CFU/mL.

When the microcrystals were synthesized with ethanol, the MIC/MBC value (31.25 µg/mL) for MRSA was lower than that observed for the microcrystals synthesized with ammonia (62.50 µg/mL). Additionally, the bactericidal activity of both β-Ag_2MoO_4 microcrystals was higher than that exhibited by the samples synthesized in water, which required higher concentration (250 µg/mL) to inhibit the MRSA growth. Figure 5a shows that, in comparison with the control (8.8 ± 0.71 $\log_{10}$ CFU/mL), at half of the MICs/MBCs values, the MRSA growth was reduced by approximately 4 logs for the β-Ag_2MoO_4 microcrystals synthesized by using ethanol (to 4.3 ± 0.07 $\log_{10}$ CFU/mL), 5 logs for the microcrystals synthesized in ammonia (to 3.9 ± 0.06 $\log_{10}$ CFU/mL), and 4 logs when water was used as the solvent (to 4.3 ± 0.07 $\log_{10}$ CFU/mL).

For *E. coli*, the microcrystals synthesized using ethanol exhibited a lower MIC/MBC value (0.49 µg/mL) than that observed for the microcrystals synthesized in ammonia (1.95 µg/mL) and water (3.91 µg/mL). The incubation of the bacteria in the presence of half of the microcrystal MICs produced a reduction of growth of approximately 5 logs for the β-Ag_2MoO_4 microcrystals, in comparison with the control (7.3 ± 0.20 $\log_{10}$ CFU/mL) and regardless of the solvent used in the synthesis (Figure 5b).

Oliveira et al. found different morphologies of Ag_2MoO_4 according to the synthesis used. When ethanol was employed, there was improvement in its antibacterial activity against the same *E. coli* strain [30]. In this study, in addition to observing better anti-*E. coli* activity for the sample synthesized in ethanol, we also tested, for the first time, the efficiency against MRSA, which is a highly pathogenic bacterium.

It is worth noting that, for the three β-Ag_2MoO_4 microcrystals obtained in water, ammonia, and ethanol, the concentrations required to kill *E. coli* were always significantly lower than those required to kill MRSA. These findings can be attributed,

at least in part, to the different cell wall structures. The Gram positive bacteria, namely, MRSA are composed of a cytoplasmic membrane and a thick, overlying peptidoglycan network (10-40 nm) composed of repeating units of a disaccharide-multipeptide building block that are polymerized and cross-linked to create a continuous network that envelops the cell [37]. This peptidoglycan network has several layers and contains mainly carboxyl, amide and hydroxyl functional groups [38], and teichoic acids (TAs). Two distinct types of TAs have been identified: wall teichoic acids (WTAs) that are linked to and embedded into the peptidoglycan, and lipoteichoic acids (LTAs) extending into and anchored to the cell membrane (cytoplasmatic membrane) [39]. On the contrary, TAs were not found in gram-negative bacterial cells, such as *E. coli* [38,39]. Additionally, although gram-negative bacteria contain an outer membrane, they only have a single peptidoglycan layer that is thin (3-6 nm) and located in the periplasmatic space between the outer membrane and the inner (cytoplasmatic) membrane [37]. Given that the cell wall is crucial to the mechanical and chemical integrity of the cells, because it protects them from the external environment and stress, all the mentioned differences between the gram-positive and gram-negative bacteria may have contributed to the higher activity of the synthesized β-Ag_2MoO_4 microcrystals against *E. coli*, in comparison to MRSA.
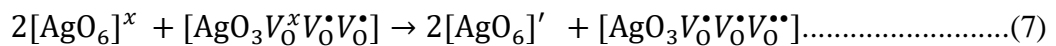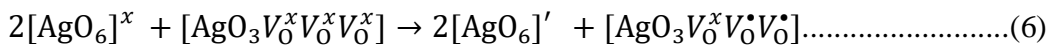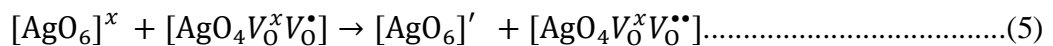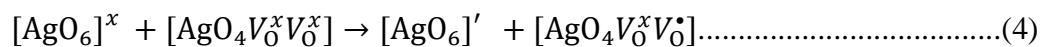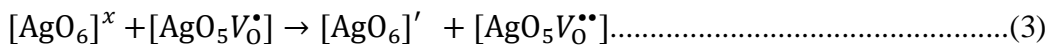
From Figures 6a, 6b, and 6c, we can see that the (111) surfaces of β-Ag_2MoO_4 were Mo, O, and Ag ion-terminated, while the (001) and (011) surfaces were O- and Ag ion-terminated. In the (111) surface, the Ag cations were coordinated to three oxygen anions to form $[AgO_3.3V_O^x]$ complex clusters, and the Mo cations were coordinated to only one oxygen anion (disfavoring its stability). The (011) surfaces exhibited the Ag cations surrounded by four oxygen anions, which resulted in the $[AgO_4.2V_O^x]$ complex clusters, while in the (001) surfaces, the silver cations were coordinated to five oxygen

anions and formed $[AgO_5.V_O^x]$ complex clusters (more stable for the electron/hole recombination processes). In addition to the atomic configuration of the exposed facets, the solvent used in the synthesis had a great effect on the reactivity and stabilization of the surfaces.

<Figure 6>

Figure 6: Mechanism of free radical formation, associated with the predominant face of the β-Ag₂MoO₄ crystal obtained in (a) water, (b) ammonia, and (c) ethanol.

A semi conductor's antibacterial activity mechanism is mainly attributed to the oxidative stress caused by the OH*, O_2', and O_2H* (reactive species) in contact with the bacterial cell wall [40,41], when $[AgO_3.3V_O^x]$, $[AgO_4.2V_O^x]$, $[AgO_5.V_O^x]$, $[AgO_6]^x$, and $[MoO_4]_o^x$ complex clusters, from which the β-Ag₂MoO₄ semiconductor is formed, are excited(Equations 1-7).

$$[MoO_4]_o^x + [MoO_4]_d^x \rightarrow [MoO_4]_o' + [MoO_4]_d^\bullet \text{...(1)}$$

$$[AgO_6]^x + [AgO_5V_O^x] \rightarrow [AgO_6]' + [AgO_5V_O^\bullet] \text{...(2)}$$

$$[AgO_6]^x + [AgO_5V_O^\bullet] \rightarrow [AgO_6]' + [AgO_5V_O^{\bullet\bullet}] \text{...(3)}$$

$$[AgO_6]^x + [AgO_4V_O^xV_O^x] \rightarrow [AgO_6]' + [AgO_4V_O^xV_O^\bullet] \text{.....................................(4)}$$

$$[AgO_6]^x + [AgO_4V_O^xV_O^\bullet] \rightarrow [AgO_6]' + [AgO_4V_O^xV_O^{\bullet\bullet}] \text{.....................................(5)}$$

$$2[AgO_6]^x + [AgO_3V_O^xV_O^xV_O^x] \rightarrow 2[AgO_6]' + [AgO_3V_O^xV_O^\bullet V_O^\bullet] \text{..........................(6)}$$

$$2[AgO_6]^x + [AgO_3V_O^xV_O^\bullet V_O^\bullet] \rightarrow 2[AgO_6]' + [AgO_3V_O^\bullet V_O^\bullet V_O^{\bullet\bullet}] \text{..........................(7)}$$
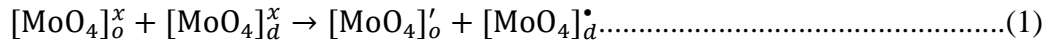
The $[AgO_5V_O^\bullet]$, $[AgO_5V_O^{\bullet\bullet}]$, $[AgO_4V_O^xV_O^\bullet]$, $[AgO_4V_O^xV_O^{\bullet\bullet}]$, $[AgO_3V_O^xV_O^\bullet V_O^\bullet]$, and $[AgO_3V_O^\bullet V_O^\bullet V_O^{\bullet\bullet}]$ complex clusters transfer a hole for water, which decomposes into a hydroxyl radical and a proton (OH* and H$^\bullet$).

Simultaneously, $[AgO_4 V_O^x V_O^\bullet]$, $[AgO_3 V_O^\bullet V_O^\bullet V_O^{\bullet\bullet}]$, $[AgO_3 V_O^x V_O^\bullet V_O^\bullet]$, $[AgO_4 V_O^x V_O^{\bullet\bullet}]$, $[MoO_4]'_o$, and $[AgO_6]'$ transfer an electron to the oxygen molecule (O_2), which produces O_2' that interacts with the proton and forms the O_2H^* radical. Figures 6a, 6b, and 6c illustrate the formation of these radicals.

According to the Wulff crystal representation of the optimized β-Ag_2MoO_4 (Figure 4), and the FE-SEM images presented in Figure 3, when β-Ag_2MoO_4 is synthetized using water, ammonia, and ethanol as the solvents, the morphologies 1, 2, and 3, respectively, are preferably obtained. This change of morphology is accompanied by the appearance of the (001) surface. When water is used as the solvent, this face is not present. However, when ammonia is used as a solvent, the (001) surface appears in the morphology. Finally, for the microcrystals synthesized in ethanol, this surface becomes more apparent. The results of the microbiological tests (MIC/MBC values and Figure 5) revealed that the antibacterial efficiency of the β-Ag_2MoO_4 microcrystals varied with the solvent used in the synthesis, and increased in the following order: water < ammonia <ethanol. Because the appearance of the (001) surface increased the antibacterial efficiency, we propose that the observed mechanism of β-Ag_2MoO_4 for the inactivation of the MRSA and *E. coli* was mainly caused by the presence of the $[AgO_5. V_O^x]$ complex clusters.

In the $[AgO_4 V_O^x V_O^\bullet]$ and $[AgO_3 V_O^x V_O^x V_O^\bullet]/[AgO_3 V_O^x V_O^\bullet V_O^\bullet]$clusters, internal electron-hole recombination can occur, while in the $[AgO_5 V_O^\bullet]$ complex clusters, the vacancy is separated from the electron because the electron is located in an $[AgO_6]'$organized complex cluster. This justifies the fact that the $[AgO_5 V_O^\bullet]$ complex clusters are more reactive and thus more effective for antibacterial applications.

Moreover, according to the Wulff crystal representation of optimized β-Ag_2MoO_4, which is shown in Figure 4, these faces have low surface energy (E_{suf} = 1.28

J/m^2), as determined by the *ab initio* calculations. Therefore, they are more easily polarized, and able to generate OH*, O$_2$′, and O$_2$H*, which are responsible for cell death.

Conclusion

We established a facile approach for the synthesis of β-Ag$_2$MoO$_4$ microcrystals with different morphology by means of the co-precipitation method and by using three different solvents (water, ammonia, and ethanol). All products exhibited powerful bactericidal capability against gram-positive bacteria, namely, MRSA, and gram-negative bacteria, namely, *E.coli*. The biocidal power increased in the following order: water <ammonia<ethanol. The relationship between the morphology of the differentβ-Ag$_2$MoO$_4$ microcrystals synthesized with different solvents, and their biological effect, was constructed systematically by combining experimental techniques and first-principle calculations. The morphologies were calculated by the Wulff crystal constructions based on first principle calculations using three surfaces: (001), (111), and (011). It was concluded that, morphologically, the larger presence of the (001) surface enhanced the antibacterial activity against the MRSA and *E. coli* bacteria. We are firmly convinced that the present study opens up the possibility for extensive investigation, not only for antimicrobial activity, but also for other applications such as the photocatalytic activity of β-Ag$_2$MoO$_4$, which can be controlled by tuning their morphology. Additionally, we expect that the results and concepts presented in this work can be extrapolated to the morphology-controlled synthesis of other materials.

Supplementary Material

Experimental Methods

Synthesis and Characterizations

The samples were synthesized as described by Fabbro et al [28]. The samples were characterized using x-ray diffraction (XRD) with a D/Max-2500PC diffractometer (Rigaku, Japan) involving CuK α radiation (λ =1.54056 Å) in the 10-70° 2θ range at a scan rate of 0.01° min^{-1}. X-ray photoelectron spectroscopy (XPS) analyses were obtained by Omicron-Scienta X-ray photoelectron spectrometer with Al Kα radiation. Micro-Raman spectroscopy was carried out by using an iHR550 spectrometer (Horiba Jobin-Yvon, Japan) with a charge-coupled device (CCD) detector and an argon-ion laser (MellesGriot, USA) operating at 633 nm with 200 mW power. The spectra were measured in the 50-1,500 cm^{-1} range. The microscopy images were analyzed using field emission gun scanning electron microscopy (FEG-SEM) on an FEI instrument (Model Inspect F50) operating at 5 kV.

Computational Methods

The Vienna ab initio Simulation Package (VASP) [42–44] was used to perform the first-principle calculations. The Kohn-Sham equations were solved by using the generalized gradient approximation (GGA) in the Perdew-Burke-Ernzerhof (PBE) functional to determine the electron exchange and correlation contributions to the total energy [45,46]. The electron-ion interaction was described within a plane wave basis set by the projector augmented wave (PAW) method [47]. The (001), (011), and (111) surfaces of β-Ag_2MoO_4 were characterized by an unreconstructed slab model using a calculated equilibrium geometry (a = 9.454 Å, and u(O) = 0.2351) and a (3×3×1) Monkhorst-Pack special k-point grid. A vacuum spacer of 15 Å was introduced in the z-direction such that the surfaces would not interact with each other [33].

E_{surf} is defined as the total energy per repeating cell of the slab (E_{slab}) minus the total energy of the perfect crystal per molecular unit (E_{bulk}) multiplied by the number of the molecular units of the surface (n), and divided by the surface area per repeating cell of the two slab sides. To confirm the convergence of the total energy with respect to the slab thickness of different surface models, E_{surf} was calculated for several low-index planes. The equilibrium shape of a crystal can be calculated by the classic Wulff construction [48], which minimizes the total surface free energy at a fixed volume, and provides a simple correlation between the surface energy (E_{surf}) of the (hkl) plane and its distance (rhkl) in the normal direction from the crystallite center.

Microbiological Tests

Microorganisms and culture conditions: Two reference strains from the American Type Culture Collection (ATCC) were used in this study to evaluate the antibacterial activity of the samples. Methicillin-resistant *Staphylococcus aureus* (MRSA – ATCC 33591) and *Escherichia coli* (*E. coli* – ATCC 8739) were maintained in a TSB medium (Acumedia Manufacturers, Inc. Baltimore, MD) and frozen at -80 ° C until use. The strains were thawed and planted on Mueller Hinton Agar (MHA) plates (Acumedia Manufacturers, Inc. Baltimore, MD), which were kept in an oven at 37 °C for 24 h-48 h until isolated colonies were formed. The bacterial inoculum was prepared as described previously [49].

Antibacterial effects of β-Ag$_2$MoO$_4$ samples obtained in different solvents: Susceptibility tests were performed according to the Clinical and Laboratory Standards Institute broth microdilution method (document M7-A7-2006) for bacteria, with modifications. The bacteria were incubated to two-fold serial dilutions of each of the β-Ag$_2$MoO$_4$ solutions in 96-well microtiter plates for 48 h at 37 °C. The material concentrations ranged from 2.000 to 0.061 μg/mL. As a positive control, the microorganisms were incubated with TSB without the addition of microcrystals, while the negative control consisted of an uninoculated culture medium. After incubation, the MIC was determined by visual inspection, and the MBC was determined by inoculating 25 μL aliquots, taken from each 96-well serial dilution and inoculated onto the MHA plates. A CFU/mL count was performed after the plates incubated at 37º C for 24h-48h. Microbiological experiments were performed on three different occasions, in triplicate.

Results and discussion

Surface compositions (XPS)

XPS survey spectra (S1) were similar among the three samples tested, and demonstrated the presence of the elements Ag, Mo, O and C. In the three samples, the silver spectrum was similar, with the $3d_{5/2}$ peak around 368 eV and the $3d_{3/2}$ peak around 374 eV. The energy difference between the peaks is about 6 eV. The data found are in accordance with the literature [50–52].
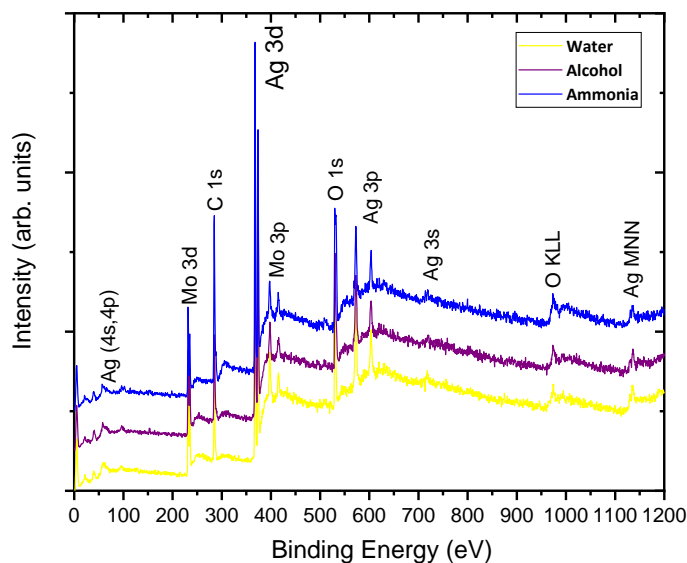
S1: XPS survey spectra of the β-Ag_2MoO_4 microcrystals synthesized in water, ethanol and ammonia.

A summary of the data obtained by XPS analysis showed no significant differences between the three synthesized samples. The binding energy of all the samples were similar for the analyzed elements.

Sample	C 1s	O 1s	Ag 3d	Mo 3d

Water	284.4 eV (C-C)	530.1 eV (O-(Mo,Ag))	367.9 eV ($3d_{5/2}$)	231.9 eV ($3d_{5/2}$)
	286.0 eV (C-(O,N))	531.4 eV (C=O-OH)	373.8 eV ($3d_{3/2}$)	234.9 eV ($3d_{3/2}$)
	287.9 eV (C-O-C;C=O)	532.9 eV (C-O)		
Ethanol	284.7 eV (C-C)	530.1 eV (O-(Mo,Ag))	367.8 eV ($3d_{5/2}$)	231.8 eV ($3d_{5/2}$)
	286.1 eV (C-(O,N))	531.4 eV (C=O-OH)	373.7 eV ($3d_{3/2}$)	234.8 eV ($3d_{3/2}$)
	288.2 eV (C-O-C;C=O)	532.9 eV (C-O)		
Ammonia	284.7 eV (C-C)	530.1 eV (O-(Mo,Ag))	367.9 eV ($3d_{5/2}$)	231.8 eV ($3d_{5/2}$)
	286.2 eV (C-(O,N))	531.6 eV (C=O-OH)	373.8 eV ($3d_{3/2}$)	234.8 eV ($3d_{3/2}$)
	288.5 eV (C-O-C;C=O)	532.8 eV (C-O)		
		533.9 eV (C-(OH,H_2O))		

S2: Summary of the XPS data of the β-Ag_2MoO_4 synthesized in water, ethanol and ammonia.

References

[1]   V.D. Araújo, R.L. Tranquilin, F. V Motta, C.A. Paskocimas, M.I.B. Bernardi, L.S. Cavalcante, J. Andres, E. Longo, M.R.D. Bomio, Effect of polyvinyl alcohol on the shape, photoluminescence and photocatalytic properties of PbMoO4 microcrystals, Mater. Sci. Semicond. Process. 26 (2014) 425–430. https://doi.org/https://doi.org/10.1016/j.mssp.2014.05.027.

[2]   M. Lei, C.X. Ye, S.S. Ding, K. Bi, H. Xiao, Z.B. Sun, D.Y. Fan, H.J. Yang, Y.G. Wang, Controllable route to barium molybdate crystal and their photoluminescence, J. Alloys Compd. 639 (2015) 102–105. https://doi.org/https://doi.org/10.1016/j.jallcom.2015.03.108.

[3]   W. Du, L. Liu, K. Zhou, X. Ma, Y. Hao, X. Qian, Black lead molybdate nanoparticles: Facile synthesis and photocatalytic properties responding to visible light, Appl. Surf. Sci. 328 (2015) 428–435. https://doi.org/https://doi.org/10.1016/j.apsusc.2014.12.068.

[4]   D. Zhang, R. Zhang, C. Xu, Y. Fan, B. Yuan, Microwave-assisted solvothermal synthesis of nickel molybdate nanosheets as a potential catalytic platform for NADH and ethanol sensing, Sensors Actuators B Chem. 206 (2015) 1–7. https://doi.org/https://doi.org/10.1016/j.snb.2014.09.013.

[5]   B.K. Maji, H. Jena, R. Asuvathraman, K.V.G. Kutty, Electrical conductivity and thermal expansion behavior of MMoO4 (M=Ca, Sr and Ba), J. Alloys Compd. 640 (2015) 475–479. https://doi.org/https://doi.org/10.1016/j.jallcom.2015.04.054.

[6]   Z. Du, H. Zhao, C. Yang, Y. Shen, C. Yan, Y. Zhang, Optimization of strontium molybdate based composite anode for solid oxide fuel cells, J. Power Sources. 274 (2015) 568–574. https://doi.org/https://doi.org/10.1016/j.jpowsour.2014.10.062.

[7]   B. Senthilkumar, R.K. Selvan, D. Meyrick, M. Minakshi, Synthesis and characterization of manganese molybdate for symmetric capacitor applications, Int. J. Electrochem. Sci. 10 (2015) 185–193.

[8]   M. Najafi, A. Abbasi, M. Masteri-Farahani, V.H.N. Rodrigues, Synthesis, characterization and crystal structure of a copper molybdate coordination polymer as an epoxidation catalyst, Inorganica Chim. Acta. 433 (2015) 21–25. https://doi.org/https://doi.org/10.1016/j.ica.2015.04.030.

[9]   K.A. Bhabu, S.R. Balaji, R. Sree Devi, T. Balu, G. Muralidharan, T.R. Rajasekaran, Investigations on growth and characterization of glycine admixture sodium molybdate crystals for nonlinear optical applications, Optik (Stuttg). 127 (2016) 1708–1713. https://doi.org/https://doi.org/10.1016/j.ijleo.2015.11.134.

[10]   C.H.B. Ng, W.Y. Fan, Uncovering Metastable α-Ag2MoO4 Phase Under Ambient Conditions. Overcoming High Pressures by 2, 3-Bis (2-pyridyl)

pyrazine Doping, Cryst. Growth Des. 15 (2015) 3032–3037.

[11]   G. da S. Sousa, F.X. Nobre, E.A. Araújo Júnior, J.R. Sambrano, A. dos R. Albuquerque, R. dos S. Bindá, P.R. da C. Couceiro, W.R. Brito, L.S. Cavalcante, M.R. de M.C. Santos, Hydrothermal synthesis, structural characterization and photocatalytic properties of β-Ag2MoO4 microcrystals: Correlation between experimental and theoretical data, Arab. J. Chem. (2018).

[12]   R.H.N. Frazão, D.G. Della Rocca, S.M. de Amorim, R.A. Peralta, C.D. Moura-Nickel, A. de Noni Jr, R. de F.P.M. Moreira, Plastic optical fibres applied on the photocatalytic degradation of phenol with Ag2MoO4 and ß-Ag2MoO4/Ag3PO4 under visible light, Environ. Technol. (2019) 1–12.

[13]   V. Kumar, S. Matz, D. Hoogestraat, V. Bhavanasi, K. Parida, K. Al-Shamery, P.S. Lee, Design of Mixed-Metal Silver Decamolybdate Nanostructures for High Specific Energies at High Power Density, Adv. Mater. 28 (2016) 6966–6975. https://doi.org/10.1002/adma.201601158.

[14]   E. Liu, W. Wang, Y. Gao, J. Jia, Tribological Properties of Adaptive Ni-Based Composites with Addition of Lubricious Ag2MoO4 at Elevated Temperatures, Tribol. Lett. 47 (2012) 21–30. https://doi.org/10.1007/s11249-012-9958-z.

[15]   T. Zhang, C. Huang, H. Lan, L. Du, W. Zhang, Tribological properties and lubrication mechanisms of a Ag–Mo composite, Lubr. Sci. 28 (2016) 141–156. https://doi.org/10.1002/ls.1306.

[16]   R. Sundaram, K.S. Nagaraja, Solid state electrical conductivity and humidity sensing studies on metal molybdate–molybdenum trioxide composites (M = Ni2+, Cu2+ and Pb2+), Sensors Actuators B Chem. 101 (2004) 353–360. https://doi.org/https://doi.org/10.1016/j.snb.2004.04.005.

[17]   S. Misra, V. Jayaraman, T. Gnanasekaran, Electrical Conductivity and Ammonia

Sensing Characteristics of Nanocrystalline Silver Molybdates Synthesized by Solution Chemistry Route, in: 2011 Int. Conf. Nanosci. Technol. Soc. Implic., 2011: pp. 1–6. https://doi.org/10.1109/NSTSI.2011.6111791.

[18]   Z.Y. Bao, D.Y. Lei, J. Dai, Y. Wu, In situ and room-temperature synthesis of ultra-long Ag nanoparticles-decorated Ag molybdate nanowires as high-sensitivity SERS substrates, Appl. Surf. Sci. 287 (2013) 404–410. https://doi.org/https://doi.org/10.1016/j.apsusc.2013.09.167.

[19]   E.K. Fodjo, D.-W. Li, N.P. Marius, T. Albert, Y.-T. Long, Low temperature synthesis and SERS application of silver molybdenum oxides, J. Mater. Chem. A. 1 (2013) 2558–2566. https://doi.org/10.1039/C2TA01018F.

[20]   A.F. Gouveia, J.C. Sczancoski, M.M. Ferrer, A.S. Lima, M.R.M.C. Santos, M.S. Li, R.S. Santos, E. Longo, L.S. Cavalcante, Experimental and Theoretical Investigations of Electronic Structure and Photoluminescence Properties of β-Ag2MoO4 Microcrystals, Inorg. Chem. 53 (2014) 5589–5599. https://doi.org/10.1021/ic500335x.

[21]   H. Jiang, J.-K. Liu, J.-D. Wang, Y. Lu, X.-H. Yang, Thermal perturbation nucleation and growth of silver molybdate nanoclusters by a dynamic template route, CrystEngComm. 17 (2015) 5511–5521. https://doi.org/10.1039/C5CE00039D.

[22]   Y.V.B. De Santana, J.E.C. Gomes, L. Matos, G.H. Cruvinel, A. Perrin, C. Perrin, J. Andrès, J.A. Varela, E. Longo, Silver Molybdate and Silver Tungstate Nanocomposites with Enhanced Photoluminescence, Nanomater. Nanotechnol. 4 (2014) 22. https://doi.org/10.5772/58923.

[23]   S.K. Gupta, P.S. Ghosh, K. Sudarshan, R. Gupta, P.K. Pujari, R.M. Kadam, Multifunctional pure and Eu3+ doped β-Ag2MoO4: photoluminescence, energy

transfer dynamics and defect induced properties, Dalt. Trans. 44 (2015) 19097–19110. https://doi.org/10.1039/C5DT03113C.

[24] X. Cui, S.-H. Yu, L. Li, L. Biao, H. Li, M. Mo, X.-M. Liu, Selective Synthesis and Characterization of Single-Crystal Silver Molybdate/Tungstate Nanowires by a Hydrothermal Process, Chem. – A Eur. J. 10 (2004) 218–223. https://doi.org/10.1002/chem.200305429.

[25] G. Nagaraju, G.T. Chandrappa, J. Livage, Synthesis and characterization of silver molybdate nanowires, nanorods and multipods, Bull. Mater. Sci. 31 (2008) 367–371. https://doi.org/10.1007/s12034-008-0057-6.

[26] J.C. Sczancoski, M.D.R. Bomio, L.S. Cavalcante, M.R. Joya, P.S. Pizani, J.A. Varela, E. Longo, M.S. Li, J.A. Andrés, Morphology and Blue Photoluminescence Emission of PbMoO4 Processed in Conventional Hydrothermal, J. Phys. Chem. C. 113 (2009) 5812–5822. https://doi.org/10.1021/jp810294q.

[27] D.P. Singh, B. Sirota, S. Talpatra, P. Kohli, C. Rebholz, S.M. Aouadi, Broom-like and flower-like heterostructures of silver molybdate through pH controlled self assembly, J. Nanoparticle Res. 14 (2012) 781. https://doi.org/10.1007/s11051-012-0781-0.

[28] M.T. Fabbro, C.C. Foggi, L.P.S. Santos, L. Gracia, A. Perrin, C. Perrin, C.E. Vergani, A.L. Machado, J. Andrés, E. Cordoncillo, E. Longo, Synthesis, antifungal evaluation and optical properties of silver molybdate microcrystals in different solvents: a combined experimental and theoretical study, Dalt. Trans. 45 (2016) 10736–10743. https://doi.org/10.1039/C6DT00343E.

[29] C. Bréchignac, P. Cahuzac, N. Kebaili, A. Lando, A. Masson, M. Schmidt, Synthesis of silver molybdate clusters driven by laser-annealing, J. Chem. Phys.

121 (2004) 9617–9622. https://doi.org/10.1063/1.1805497.

[30]   C.A. Oliveira, D.P. Volanti, A.E. Nogueira, C.A. Zamperini, C.E. Vergani, E. Longo, Well-designed β-Ag2MoO4 crystals with photocatalytic and antibacterial activity, Mater. Des. 115 (2017) 73–81. https://doi.org/https://doi.org/10.1016/j.matdes.2016.11.032.

[31]   C.H.B. Ng, W.Y. Fan, Crystal Origami: Preparation of β-Ag2MoO4 Concave and Convex Crystals with High-Index Facets, ChemNanoMat. 3 (2017) 178–182. https://doi.org/10.1002/cnma.201600362.

[32]   J. Davies, D. Davies, Origins and evolution of antibiotic resistance, Microbiol. Mol. Biol. Rev. 74 (2010) 417–433.

[33]   M.T. Fabbro, C. Saliby, L.R. Rios, F.A. La Porta, L. Gracia, M.S. Li, J. Andrés, L.P.S. Santos, E. Longo, Identifying and rationalizing the morphological, structural, and optical properties of β-Ag2MoO4 microcrystals, and the formation process of Ag nanoparticles on their surfaces: combining experimental data and first-principles calculations, Sci. Technol. Adv. Mater. 16 (2015) 65002. https://doi.org/10.1088/1468-6996/16/6/065002.

[34]   J.V. Kumar, R. Karthik, S.-M. Chen, V. Muthuraj, C. Karuppiah, Fabrication of potato-like silver molybdate microstructures for photocatalytic degradation of chronic toxicity ciprofloxacin and highly selective electrochemical detection of H 2 O 2, Sci. Rep. 6 (2016) 34149.

[35]   J. Andrés, M.M. Ferrer, L. Gracia, A. Beltran, V.M. Longo, G.H. Cruvinel, R.L. Tranquilin, E. Longo, A Combined Experimental and Theoretical Study on the Formation of Ag Filaments on β-Ag2MoO4 Induced by Electron Irradiation, Part. Part. Syst. Charact. 32 (2015) 646–651. https://doi.org/10.1002/ppsc.201400162.

[36] M.A. Wikler, Methods for dilution antimicrobial susceptibility tests for bacteria that grow aerobically: approved standard, CLSI. 26 (2006) M7-A7.

[37] A.J.F. Egan, R.M. Cleverley, K. Peters, R.J. Lewis, W. Vollmer, Regulation of bacterial cell wall growth, FEBS J. 284 (2017) 851–867. https://doi.org/10.1111/febs.13959.

[38] W. Jiang, A. Saxena, B. Song, B.B. Ward, T.J. Beveridge, S.C.B. Myneni, Elucidation of functional groups on gram-positive and gram-negative bacterial surfaces using infrared spectroscopy, Langmuir. 20 (2004) 11433–11442.

[39] T. SHIRAISHI, S. YOKOTA, S. FUKIYA, A. YOKOTA, Structural diversity and biological significance of lipoteichoic acid in Gram-positive bacteria: focusing on beneficial probiotic lactic acid bacteria, Biosci. Microbiota, Food Heal. 35 (2016) 147–161. https://doi.org/10.12938/bmfh.2016-006.

[40] O.K. Dalrymple, E. Stefanakos, M.A. Trotz, D.Y. Goswami, A review of the mechanisms and modeling of photocatalytic disinfection, Appl. Catal. B Environ. 98 (2010) 27–38. https://doi.org/https://doi.org/10.1016/j.apcatb.2010.05.001.

[41] Y. Li, W. Zhang, J. Niu, Y. Chen, Mechanism of Photogenerated Reactive Oxygen Species and Correlation with the Antibacterial Properties of Engineered Metal-Oxide Nanoparticles, ACS Nano. 6 (2012) 5164–5173. https://doi.org/10.1021/nn300934k.

[42] G. Kresse, J. Furthmüller, Efficiency of ab-initio total energy calculations for metals and semiconductors using a plane-wave basis set, Comput. Mater. Sci. 6 (1996) 15–50. https://doi.org/https://doi.org/10.1016/0927-0256(96)00008-0.

[43] G. Kresse, J. Furthmüller, Efficient iterative schemes for ab initio total-energy calculations using a plane-wave basis set, Phys. Rev. B. 54 (1996) 11169–11186. https://doi.org/10.1103/PhysRevB.54.11169.

[44] G. Kresse, D. Joubert, From ultrasoft pseudopotentials to the projector augmented-wave method, Phys. Rev. B. 59 (1999) 1758–1775. https://doi.org/10.1103/PhysRevB.59.1758.

[45] J.P. Perdew, K. Burke, M. Ernzerhof, Generalized Gradient Approximation Made Simple, Phys. Rev. Lett. 77 (1996) 3865–3868. https://doi.org/10.1103/PhysRevLett.77.3865.

[46] J.P. Perdew, J.A. Chevary, S.H. Vosko, K.A. Jackson, M.R. Pederson, D.J. Singh, C. Fiolhais, Atoms, molecules, solids, and surfaces: Applications of the generalized gradient approximation for exchange and correlation, Phys. Rev. B. 46 (1992) 6671–6687. https://doi.org/10.1103/PhysRevB.46.6671.

[47] P.E. Blöchl, Projector augmented-wave method, Phys. Rev. B. 50 (1994) 17953–17979. https://doi.org/10.1103/PhysRevB.50.17953.

[48] G. Wulff, Xxv. zur frage der geschwindigkeit des wachsthums und der auflösung der krystallflächen, Zeitschrift Für Krist. Mater. 34 (1901) 449–530.

[49] C.C. de Foggi, R.C. de Oliveira, M.T. Fabbro, C.E. Vergani, J. Andres, E. Longo, A.L. Machado, Tuning the Morphological, Optical, and Antimicrobial Properties of α-Ag2WO4 Microcrystals Using Different Solvents, Cryst. Growth Des. 17 (2017) 6239–6246. https://doi.org/10.1021/acs.cgd.7b00786.

[50] Y.J. Oh, J.J. Yoo, Y. Il Kim, J.K. Yoon, H.N. Yoon, J.-H. Kim, S. Bin Park, Oxygen functional groups and electrochemical capacitive behavior of incompletely reduced graphene oxides as a thin-film electrode of supercapacitor, Electrochim. Acta. 116 (2014) 118–128.

[51] D.G. Larrude, M.E.H. Costa, Synthesis and characterization of silver nanoparticle-multiwalled carbon nanotube composites, J. Nanomater. 2014 (2014) 90.

[52] J.-W. Shi, Y. Zou, D. Ma, Z. Fan, L. Cheng, D. Sun, Z. Wang, C. Niu, L. Wang,

Stable 1T-phase MoS 2 as an effective electron mediator promoting

photocatalytic hydrogen production, Nanoscale. 10 (2018) 9292–9303.